Monthly Notices of the ROYAL ASTRONOMICAL SOCIETY
MNRAS **453,** 3414–3427 (2015) doi:10.1093/mnras/stv1874

Mass-loss from advective accretion disc around rotating black holes

Ramiz Aktar,[1⋆] Santabrata Das[1⋆] and Anuj Nandi[2⋆]

[1]*Indian Institute of Technology Guwahati, Guwahati 781039, India*
[2]*Space Astronomy Group, SSIF/ISITE Campus, ISRO Satellite Centre, Outer Ring Road, Marathahalli, Bangalore 560037, India*

Accepted 2015 August 11. Received 2015 August 11; in original form 2015 June 9

ABSTRACT

We examine the properties of the outflowing matter from an advective accretion disc around a spinning black hole. During accretion, rotating matter experiences centrifugal pressure-supported shock transition that effectively produces a virtual barrier around the black hole in the form of post-shock corona (hereafter PSC). Due to shock compression, PSC becomes hot and dense that eventually deflects a part of the inflowing matter as bipolar outflows because of the presence of extra thermal gradient force. In our approach, we study the outflow properties in terms of the inflow parameters, namely specific energy ($\mathcal{E}$) and specific angular momentum (λ) considering the realistic outflow geometry around the rotating black holes. We find that spin of the black hole (a_k) plays an important role in deciding the outflow rate $R_{\dot{m}}$ (ratio of mass flux of outflow to inflow); in particular, $R_{\dot{m}}$ is directly correlated with a_k for the same set of inflow parameters. It is found that a large range of the inflow parameters allows global accretion–ejection solutions, and the effective area of the parameter space ($\mathcal{E}$, λ) with and without outflow decreases with black hole spin (a_k). We compute the maximum outflow rate ($R_{\dot{m}}^{\rm max}$) as a function of black hole spin (a_k) and observe that $R_{\dot{m}}^{\rm max}$ weakly depends on a_k that lies in the range ∼10–18 per cent of the inflow rate for the adiabatic index (γ) with $1.5 \geq \gamma \geq 4/3$. We present the observational implication of our approach while studying the steady/persistent jet activities based on the accretion states of black holes. We discuss that our formalism seems to have the potential to explain the observed jet kinetic power for several Galactic black hole sources and active galactic nuclei.

Key words: accretion, accretion discs – black hole physics – shock waves – ISM: jets and outflows – X-rays: binaries.

1 INTRODUCTION

Powerful jets and outflows are commonly observed in accreting black hole (BH) systems including active galactic nuclei (AGNs) and X-ray binaries (Mirabel et al. 1992; Mirabel & Rodriguez 1994, 1998; Hjellming & Rupen 1995; Ferrari 1998; Junor, Biretta & Livio 1999; Cheung 2002; Mirabel 2003; Miller et al. 2012). In spite of the availability of wealth of high-resolution observations, the physical mechanism of jet generation and its powering processes are still remain unclear. However, the obvious cause seems to be the extreme gravity that powers the outflows where spin of the central objects may play an important role in producing the relativistic jets. Earlier work of Penrose (1969) demonstrated that infalling particles on to a rotating BH have the potential to extract some of the rotational energy of the BHs. Close to the horizon, space–time geometry is dragged due to BH rotation and the magnetic field lines are twisted resulting into the transport of energy from the BH along the field lines. Blandford & Znajek (1977) showed that this purely electromagnetic energy extraction mechanism via the threading of magnetic field lines has the potential to power the jets. This appealing mechanism clearly indicates that BH spin perhaps plays an important role to produce jets in BH systems. In order to establish this feature observationally, attempts have been made to find the evidence of spin-powered jets for the stellar mass BHs. According to Steiner, McClintock & Narayan (2013) and McClintock, Narayan & Steiner (2014), significant positive correlation between the radio luminosity associated with the mechanical power of ballistic jets and the spin of the BH is seen when the transient BH systems are fed at Eddington-limited accretion rates. However, Russell, Gallo & Fender (2013) and Fender & Gallo (2014) ruled out the direct evidence of any such correlation between the transient jet power and the BH spin. Using radio–optical correlation, van Velzen & Falcke (2013) also reported that the BH spin possibly does not have any dominant role in powering the jets. In a numerical endeavour, De Villiers et al. (2005) claimed that the jet efficiency increases by two orders of magnitude for rapidly rotating BH compared to the non-spinning BH. In the similar context, Fernández et al. (2015)

⋆ E-mail: ramiz@iitg.ernet.in (RA); sbdas@iitg.ernet.in (SD); anuj@isac.gov.in (AN)

showed that the more mass is evacuated from the disc as the BH spin is increased. In an early effort, Donea & Biermann (1996) also found that the jet power is strongly dependent on the spin of the BHs without considering the jet geometry. Overall, all the above findings are in contrast and therefore inconclusive.

Meanwhile, some authors pointed out that there exists a confirm connection between the accretion spectral states and the jet states (i.e. thick and thin) in BH systems, particularly for microquasars (Gallo, Fender & Pooley 2003; Rushton et al. 2010). In the low-hard spectral states (LHS) of galactic black holes (GBHs), quasi-steady and persistent jets are observed, whereas relatively stronger jets are launched generally in the hard-intermediate state (HIMS). In addition, transient relativistic ejections are observed during the state transition from hard-intermediate to soft-intermediate state (SIMS) (Fender, Belloni & Gallo 2004; Fender, Homan & Belloni 2009). Interestingly, jet activities are not seen in the high-soft states. It has also been observed that during ejections, quasi-periodic oscillations (QPOs) are not observed and energy spectra get softens (Vadawale et al. 2001; Miller-Jones et al. 2012; Radhika & Nandi 2014). This is conjectured in a way that the matter is ejected from the inner part of the disc [i.e. Compton corona equivalently post-shock corona (PSC)] (Feroci et al. 1999; Nandi et al. 2001b; Chakrabarti et al. 2002). Towards this, very recently, Radhika & Nandi (2014) reported the inflow–outflow connection through the observation in *radio* and *X-ray* bands for the object XTE J1859+226 and claimed that the fast variation of the 'spectro-temporal' properties of outbursting GBHs is connected with the disruption of the post-shock disc (i.e. PSC) in terms of evacuation of matter in the form of jets (Radhika, Nandi & Seetha, in preparation). They pointed out that the QPOs are not seen during 'transient' ejection of jets observed in *radio*. This result indicates that PSC possibly is responsible for the origin of QPOs in GBHs (Chakrabarti & Manickam 2000; Nandi et al. 2001a,b). When jets are emerged out at the cost of the evacuation/disruption of PSC, QPOs are missing (Vadawale et al. 2001; Radhika & Nandi 2014). Extensive magnetohydrodynamic simulations of accretion disc around rotating BHs also indicate that windy hot materials (i.e. corona) blow away from the inner part of the disc as jets (Koide et al. 2002; McKinney & Gammie 2004; De Villiers et al. 2005). Meanwhile, Das et al. (2014) showed that PSC modulates quasi-periodically when viscosity parameter is chosen to its critical value and such modulation successfully exhibits quasi-periodic variation of PSC as well as the outflow rates. These scenarios indicate that there seems to be direct correlation between PSC and outflow. Based on these correlations, one can conjecture that the disc–jet symbiosis is strongly coupled and advective accreting disc perhaps is responsible for the launching of jets and outflows.

Advective accretion flow around the BHs must be transonic in order to satisfy the inner boundary conditions. Inflowing matter experiences a virtual barrier in the vicinity of the BH due to centrifugal repulsion against gravity. According to the second law of thermodynamics, such a virtual barrier triggers the discontinuous transition of the flow variables in the form of shock wave in order to prefer the high-entropy solution when possible (Fukue 1987; Chakrabarti 1989; Lu, Gu & Yuan 1999; Becker & Kazanas 2001; Fukumura & Tsuruta 2004). Due to compression, the shock-induced accretion flow produces hot and dense PSC surrounding the BHs which essentially acts as the effective boundary layer of the BHs. During accretion, a part of the inflowing matter is deflected by PSC which is further driven out in the vertical direction by the excess thermal gradient force across the shock, producing bipolar outflows. Such an appealing mechanism to launch outflow from the vicinity of the BH has been confirmed through numerical simulations (Molteni, Lanzafame & Chakrabarti 1994; Molteni, Ryu & Chakrabarti 1996; Machida, Hayashi & Matsumoto 2000; De Villiers et al. 2005; Das et al. 2014; Okuda 2014; Okuda & Das 2015). In addition, numerous attempts have been made theoretically to calculate the mass outflow rate around BHs. Chakrabarti (1999) calculated the mass outflow rate considering isothermal flow. Using both Keplerian and sub-Keplerian components, Das et al. (2001a) self-consistently estimated mass-loss from the disc and found that the outflow rate strongly depends on both components. Singh & Chakrabarti (2011) implemented the energy dissipation across the shock while obtaining the outflow rate and found that possibility of mass-loss anti-correlates with the dissipation rate. Following the work of Molteni et al. (1996), several authors (Chattopadhyay & Das 2007; Das & Chattopadhyay 2008; Kumar & Chattopadhyay 2013; Kumar et al. 2013; Das et al. 2014) studied the properties of mass outflow rate in terms of inflow parameters considering dissipative accretion flow. However, all these works were carried out with limitation as spin of the BH was not considered.

Motivating with this, we model the inflow–outflow activity around a rotating BH. Since the PSC is induced by the shock transition itself, we self-consistently calculate the properties of shock-driven outflows in terms of the inflow parameters and investigate the effect of the BH spin on it. For simplicity, we adopt the pseudo-Kerr potential proposed by Chakrabarti & Mondal (2006) to describe the space–time geometry around the BH. This potential accurately reproduces the particle trajectories around rotating BHs having spin $a_k \lesssim 0.8$. We calculate the global accretion solutions in the presence of thermally driven outflows and obtain the parameter spaces spanned by energy and angular momentum of the inflowing matter in terms of the BH spin. We observe that the shock-induced global inflow–outflow solutions exist for a wide range of inflow parameters. Varying the inflow parameters, we estimate the *maximum mass outflow rate* ($R_{\dot{m}}^{\max}$) as a function of BH spin (a_k) and find that $R_{\dot{m}}^{\max}$ weakly depends on a_k having highest value ∼17–18 per cent of the inflow rate for $\gamma = 4/3$. Further, we calculate the *unabsorbed* X-ray flux of several BH objects using the *RXTE*[1] satellite archival data and obtain their accretion rates considering the accretion efficiency $\eta = 0.3$ (Thorne 1974), which perhaps is reasonable for rotating BHs. With this, using our theoretical estimate of maximum mass outflow rate, we then compute the maximum jet kinetic power ($L_{\rm jet}^{\max}$). These results are further compared with those available from observations, and close agreements are seen. Following this, our theoretical prediction essentially provides an estimate of $L_{\rm jet}^{\max}$ for those sources for which observed jet power is uncertain.

In the next section, we describe the basic assumptions and the governing equations for our model. In Section 3, we discuss the methodology to calculate the mass outflow rates self-consistently. In Section 4, we present the results which is followed by discussions. In Section 5, we apply our formalism to calculate the jet kinetic power for several astrophysical objects (GBHs and AGNs). Finally in Section 6, we draw the concluding remarks.

2 MODEL EQUATIONS AND ASSUMPTIONS

We consider an axisymmetric disc–jet system around a rotating BH in the steady state. Here, the accretion disc lies along the BH equatorial plane while the jet geometry is described about the BH rotation axis. In this work, we mainly focus on the inner region of

[1] http://www.heasarc.gsfc.nasa.gov

the accretion disc, where the viscous time-scale is larger than the infall time-scale and therefore, the angular momentum transport due to the differential motion is weakly significant leaving the flow to be inviscid there (Chakrabarti 1989). Further, in our model, jets are originated from the inner part of the accretion disc (PSC) with the same angular momentum of the disc as we neglect the effect of resulting torque in the disc–jet system. Next, we present the governing equations that describe the fluid properties of the accretion disc and the jets. All the equations are written in geometric unit system as $G = M_{\rm BH} = c = 1$, where, G is the gravitational constant, $M_{\rm BH}$ is the black hole mass and c is the speed of light, respectively. In this system, the units of length, mass and time are expressed as $GM_{\rm BH}/c^2$, $M_{\rm BH}$ and $GM_{\rm BH}/c^3$.

2.1 Governing equations for accretion

We consider a geometrically thin, axisymmetric, low angular momentum, advective accretion flow around a rotating BH. For simplicity, we adopt the pseudo-Kerr effective potential introduced by Chakrabarti & Mondal (2006) to represent the space–time geometry around the BH instead of using full general relativistic prescription. This enables us to solve the problem following the Newtonian approach and keeping all the salient features of space–time geometry around it. The equation of motion describing the accreting matter is given by

(i) the energy conservation equation:

$$\mathcal{E} = \frac{v^2}{2} + \frac{a^2}{\gamma - 1} + \Phi, \tag{1}$$

where $\mathcal{E}$ represents the specific energy of the flow, v is the radial velocity and a is the adiabatic sound speed defined as $a = \sqrt{\gamma P/\rho}$. Here, P is the isotropic pressure, ρ is the gas density and γ is the adiabatic index, respectively. The accreting gas is described by the adiabatic equation of state as $P = K\rho^{\gamma}$, where K is the measure of specific entropy, which is constant except at the shock transition. The effective potential Φ is given by (Chakrabarti & Mondal 2006)

$$\Phi = -\frac{B + \sqrt{B^2 - 4AC}}{2A}, \tag{2}$$

where

$$A = \frac{\alpha^2\lambda^2}{2x^2},$$

$$B = -1 + \frac{\alpha^2\omega\lambda r^2}{x^2} + \frac{2a_k\lambda}{r^2 x},$$

$$C = 1 - \frac{1}{r - x_0} + \frac{2a_k\omega}{x} + \frac{\alpha^2\omega^2 r^4}{2x^2}.$$

Here, x and r represent the cylindrical and spherical radial distance considering that the BH is located at the origin of the coordinate system and λ is the specific angular momentum of the flow. Here, $x_0 = 0.04 + 0.97a_k + 0.085a_k^2$, $\omega = 2a_k/(x^3 + a_k^2 x + 2a_k^2)$ and $\alpha^2 = (x^2 - 2x + a_k^2)/(x^2 + a_k^2 + 2a_k^2/x)$, where α is the redshift factor and a_k represents the BH rotation parameter defined as the specific spin angular momentum of the BH. According to Chakrabarti & Mondal (2006), the above potential mimics the Kerr geometry quite satisfactorily for a wide range of $a_k \lesssim 0.8$.

(ii) The mass conservation equation:

$$\dot{M} = 4\pi\rho v x h, \tag{3}$$

where $\dot{M}$ denotes the mass accretion rate which is constant everywhere except the region of mass-loss and h is the half-thickness of the disc obtained from thin disc approximation (Chakrabarti 1989) as

$$h(x) = a\sqrt{\frac{x}{\gamma\Phi_r^{'}}}. \tag{4}$$

Here $\Phi_r^{'} = (\partial\Phi/\partial r)_{z\ll x}$, z is the vertical height in the cylindrical coordinate system and $r = \sqrt{x^2 + z^2}$.

Combining the expression of sound speed and the adiabatic equation of the state of the gas, we calculate the entropy accretion rate as (Chakrabarti 1990)

$$\dot{\mathcal{M}} = va^{\nu}\sqrt{\frac{x^3}{\gamma\Phi_r^{'}}}, \tag{5}$$

where $\nu = (\gamma + 1)/(\gamma - 1)$. In an accretion disc, $\dot{\mathcal{M}}$ remains constant all throughout except at the shock transition where local turbulence generates entropy. Therefore, the entropy accretion rate in the post-shock region is higher than that in the pre-shock region.

By definition, the accretion flow around the BHs must be transonic in nature. This is due to the fact that the velocity of the accreting matter at large distances from the BH is negligibly small and therefore, the flow is subsonic. However, flow crosses the event horizon with velocity equivalent to the speed of light implying that the flow is supersonic close to the BH. This clearly indicates that the accretion flow necessarily changes its sonic state during its journey from the outer edge of the disc to the horizon. In order to calculate the location where the state of this sonic transition occurs, we derive the sonic point conditions using equations (1)–(5) and obtain

$$\frac{{\rm d}v}{{\rm d}x} = \frac{N}{D}, \tag{6}$$

where

$$N = \frac{a^2}{\gamma + 1}\left[\frac{3}{x} - \frac{{\rm d}\ln\Phi_r^{'}}{{\rm d}x}\right] - \frac{{\rm d}\Phi_{\rm e}}{{\rm d}x} \tag{7}$$

and

$$D = v - \frac{2a^2}{(\gamma + 1)v}. \tag{8}$$

Here, the subscript 'e' signifies the quantity measured at the disc equatorial plane. Since the accretion flow is smooth everywhere, the radial velocity gradient must be finite everywhere too. According to equation (6), if the denominator D vanishes at any radial distance, the numerator N also vanishes there. Such a location, where $D = N = 0$, is called as sonic point. Setting $D = 0$ and $N = 0$ independently, we find the sonic point conditions as

$$D = 0 \Rightarrow M_{\rm c} = \frac{v_{\rm c}}{a_{\rm c}} = \sqrt{\frac{2}{\gamma + 1}} \tag{9}$$

and

$$N = 0 \Rightarrow a_{\rm c}^2 = (\gamma + 1)\left(\frac{{\rm d}\Phi_{\rm e}}{{\rm d}x}\right)_{\rm c}\left[\frac{3}{x} - \frac{{\rm d}\ln\Phi_r^{'}}{{\rm d}x}\right]_{\rm c}^{-1}. \tag{10}$$

Here, the subscript 'c' denotes the quantities evaluated at the sonic points. We use sonic point conditions, namely equations (9) and (10), in equation (1) to obtain the location of sonic point for a given set of $(\mathcal{E}, \lambda)$ of the flow. For a physically acceptable transonic solution, flow must contain at least one saddle-type sonic point (Das 2007 and references therein). Depending on the values of $\mathcal{E}$ and λ, flow may possess multiple sonic points as well which is one of the necessary condition to form a shock wave (Chakrabarti 1990). At the sonic point, equation (6) takes the form as ${\rm d}v/{\rm d}r = 0/0$

and therefore, we use l'Hospital rule to calculate the radial velocity gradient there. Once the flow variables at the sonic point are known, we integrate equation (6) starting from the sonic point inwards up to the BH horizon and outwards to a large distance to obtain the full set of global accretion solution which may own standing shock waves.

2.2 Governing equations for outflow

In this work, we consider the outflow to be emerged out from the accretion disc along the rotation axis of the BH with the same energy and angular momentum as the accretion flow since we neglect the dissipative processes (i.e. viscosity, cooling, etc.). Similar to accretion flow, we consider the outflow to obey the polytropic equation of state as $P_j = K_j \rho_j^{\gamma}$, where the subscript '$j$' denotes the outflow variables. The equations of motion that describe the outflow dynamics are given by

(i) the energy conservation equation of outflow:

$$\mathcal{E}_j = \frac{1}{2} v_j^2 + \frac{a_j^2}{\gamma - 1} + \Phi, \tag{11}$$

where $\mathcal{E}_j$ ($\equiv \mathcal{E}$) represents the specific energy of the outflow, v_j is the outflow velocity and a_j is the sound speed of the outflow, respectively.

(ii) Mass conservation equation of outflow:

$$\dot{M}_{\rm out} = \rho_j v_j \mathcal{A}, \tag{12}$$

where $\mathcal{A}$ is a geometrical quantity representing the total area function of the outflow. To obtain $\mathcal{A}$, we consider the outflow geometry as described in Molteni et al. (1996) where the outflowing matter tends to come out through the two surfaces, namely the centrifugal barrier (CB) and the funnel wall (FW). We calculate the CB by identifying the pressure maxima surface as $(\mathrm{d}\Phi/\mathrm{d}x)_{r_{\rm CB}} = 0$ and the FW by defining the null effective potential as $\Phi|_{r_{\rm FW}} = 0$ (Molteni et al. 1996). As the effective potential of our interest is complex in nature, it is unattainable to prevail an analytical expression of the CB surface and the FW and therefore, we compute them numerically. In Fig. 1, we illustrate the outflow geometry around the rotating BHs for a wide range of a_k marked in the figure and compare them with the same obtained using the pseudo-Newtonian potential introduced by Paczyński & Wiita (1980) appropriate for a stationary BH. The regions bounded by the dashed and dotted curves are for $a_k = -0.998$ and 0.8, respectively, and the solid curves depict the result of stationary BH. Note that the outflow geometry for stationary as well as for rotating BHs is indistinguishable outside the range of few tens of Schwarzschild radius. This is possibly due to the fact that the effect of BH spin on the space–time geometry cursorily diminishes with the increasing distances. Keeping this in mind, we therefore adopt the outflow geometry of the stationary BH for our present study in order to avoid the rigorous numerical calculations. This enables us to obtain an analytical expression of area function $\mathcal{A}$ and its higher order derivatives, which is required in the sonic point analysis of outflowing matter (Das & Chattopadhyay 2008). A comprehensive study of sonic point analysis for outflows including the area function $\mathcal{A}$ and its derivatives has already been presented in Das & Chattopadhyay (2008) and therefore, we avoid repetition here.

3 SOLUTION METHODOLOGY

In this study, we consider the post-shock matter (PSC) as the precursor of the jet base and thus, we focus only on those accretion solutions that possess standing shock waves. For shock, the accretion flow variables experience discontinuous transition characterized by the Rankine–Hugoniot (hereafter R-H) shock conditions (Landau & Lifshitz 1959). These conditions include the conservations of mass flux, energy flux and momentum flux across the shock, respectively. In the presence of mass-loss, a part of the inflowing matter is effectively emerged out as outflow from the post-shock region (PSC), while the remaining matter is advected into the BH straight away. Therefore, in the present scenario, the shock conditions are given by

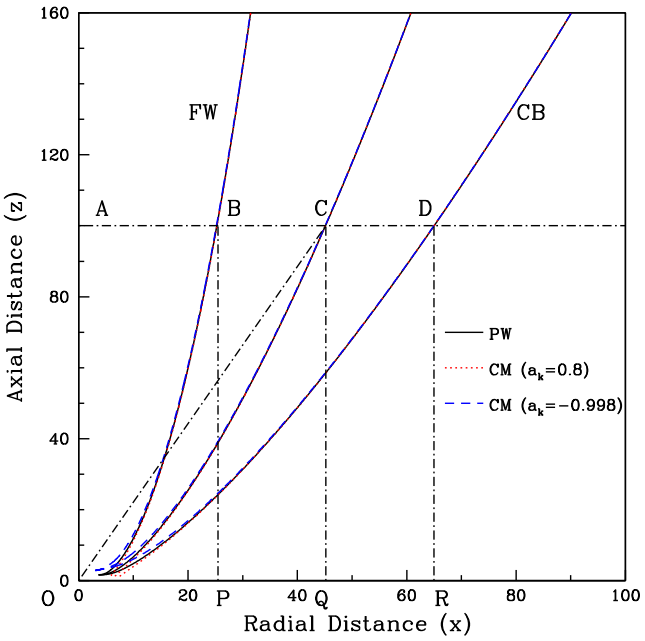

Figure 1. Comparison of jet geometry for angular momentum $\lambda = 3.3$. Funnel wall (FW) and centrifugal barrier (CB) are marked in the figure. Here, OC $= r_j$ is the spherical radius representing the streamline of the outflow. Dashed and dotted curves are obtained for $a_k = -0.998$ and 0.8, while solid curve denotes the result obtained using pseudo-Newtonian potential (Paczyński & Wiita 1980). Jet geometries for stationary as well as rotating BHs are indistinguishable beyond few tens of Schwarzschild radius. See the text for details.

(i) Conservation of mass flux:

$$\dot{M}_+ = \dot{M}_- - \dot{M}_{\rm out} = \dot{M}_-(1 - R_{\dot{m}}). \tag{13a}$$

The quantities having subscripts '$-$' and '$+$' are referred to the values before and after the shock which we follow throughout the paper unless otherwise stated. The pre-shock and post-shock accretion rates are denoted by $\dot{M}_-$ and $\dot{M}_+$, respectively, and $\dot{M}_{\rm out}$ is the mass flux for the outflowing matter. Following this, the mass outflow rate is computed as $R_{\dot{m}} = \dot{M}_{\rm out}/\dot{M}_-$. The next condition is

(ii) Conservation of energy flux:

$$\mathcal{E}_+ = \mathcal{E}_-, \tag{13b}$$

and finally, we have

(iii) Conservation of momentum flux:

$$W_+ + \Sigma_+ v_+^2 = W_- + \Sigma_- v_-^2, \tag{13c}$$

where W and Σ represent the vertically integrated pressure and density (Das, Chattopadhyay & Chakrabarti 2001b).

We rewrite equations (13b) and (13c) in terms of Mach number ($M = v/a$) and are given by

$$\frac{1}{2}M_+^2 a_+^2 + \frac{a_+^2}{\gamma - 1} = \frac{1}{2}M_-^2 a_-^2 + \frac{a_-^2}{\gamma - 1} \tag{13d}$$

and

$$\left[\frac{2a_+}{(3\gamma - 1)M_+} + M_+ a_+\right] = \frac{1}{1 - R_{\dot{m}}}\left[\frac{2a_-}{(3\gamma - 1)M_-} + M_- a_-\right], \tag{13e}$$

where we utilize equation (13a) and $a = \sqrt{(3\gamma - 1)W/(2\Sigma)}$ (Das et al. 2001b).

Using equations (13d) and (13e), we obtain a shock-invariant quantity (C_s) in terms of Mach number M as

$$C_s = \frac{\left[\frac{2}{M_+} + (3\gamma - 1)M_+\right]^2 (1 - R_{\dot{m}})^2}{\left[2 + (\gamma - 1)M_+^2\right]} = \frac{\left[\frac{2}{M_-} + (3\gamma - 1)M_-\right]^2}{\left[2 + (\gamma - 1)M_-^2\right]},$$

where M_- and M_+ stand for Mach number just before and after the shock in the pre-shock and post-shock flow, respectively.

Since the shock conditions are coupled with inflow and outflow variables, the accretion and jet equations are solved simultaneously. We obtain the jet velocity gradient from its governing equations and calculate the sonic point properties following the 'critical point' analysis (Chakrabarti 1989). While doing this, we use the inflow parameters, namely energy $\mathcal{E}$ and angular momentum λ of the inflow. This is because the outflow is considered to be originated from the post-shock region (PSC). This also ensures that the jets are launched with the same density as the post-shock flow, namely $\rho_j = \rho_+$. Further, we integrate the jet equations to calculate the outflow variables at the jet base starting from the jet sonic point, and using equations (3), (4) and (12) we compute the mass outflow rate in terms of the inflow–outflow properties at the shock and is given by

$$R_{\dot{m}} = \frac{\dot{M}_{\rm out}}{\dot{M}_-} = \frac{\rho_j v_j(x_s)\mathcal{A}(x_s)}{4\pi\rho_- v_- x_s h_-} = \frac{R v_j(x_s)\mathcal{A}(x_s)}{4\pi\sqrt{\frac{1}{\gamma}}x_s^{3/2}\Phi_r^{'-1/2}a_+ v_-}, \tag{14}$$

where $R = \Sigma_+/\Sigma_-(\equiv \rho_+ h_+/\rho_- h_- = \rho_j a_+/\rho_- a_-)$ is the compression ratio, and $v_j(x_s)$ and $\mathcal{A}(x_s)$ are the jet velocity and the jet area function at the shock, respectively. We utilize an iterative method to calculate $R_{\dot{m}}$ self-consistently which is given as follows.

We begin with $R_{\dot{m}} = 0$. Using the shock-invariant quantity, we calculate the virtual shock location x_s^v for a given set of ($\mathcal{E}$, λ) with the consideration that the entropy of the inflowing post-shock matter ($\dot{\mathcal{M}}_+$) and outflowing matter ($\dot{\mathcal{M}}_{\rm out}$) is larger than the entropy of the pre-shock matter ($\dot{\mathcal{M}}_-$). This eventually reflects the fact of the second law of thermodynamics as the shocked solutions ascertain the preferred mode of accretion. We use the same set of inflow parameters for jet equations and calculate $R_{\dot{m}}$ which we employ further in the shock-invariant equation to obtain a new shock location. We continue this iteration process until the solution converges to the actual shock location and accordingly we compute the corresponding $R_{\dot{m}}$. In the following sections, we investigate the properties of x_s and $R_{\dot{m}}$ in terms of the inflow parameters ($\mathcal{E}$, λ) for various values of BH spin (a_k) and present the results which are followed by the discussion on astrophysical applications.

4 RESULTS AND DISCUSSIONS

In an advective accretion process around BHs, the accreting matter suffers discontinuous shock transitions due to the CB. This causes the post-shock flow to become hot and puffed up which eventually behaves like a effective boundary layer around the BH (i.e. PSC). During accretion, a part of the inflowing matter is deflected vertically by this boundary layer to produce thermally driven outflows. To illustrate the complete picture of the accretion and ejection mechanism, we present the global inflow–outflow solutions for various a_k in Fig. 2. In panels (a), (b) and (c), we show the variation of Mach number ($M = v/a$) of the inflow with the radial distance (x) for $a_k = 0.8$, 0.0 and -0.998, respectively. Subsonic matter at large distance gradually gains its radial velocity as it proceeds towards the BH due to the fatal attraction of gravity and crosses the outer sonic point ($x_{\rm out}$) to become supersonic as shown by the arrows. As the flow continues its journey further towards the BH, it experiences discontinuous transition in flow variables when the R-H conditions are favourable which is indicated by the dashed vertical arrow. After this transition, flow momentarily slows down and gradually picks up its velocity. Eventually, flow becomes supersonic again after crossing the inner sonic point ($x_{\rm in}$) and finally enters into the BH. As the outflow is emerged out from the effective boundary layer of the BH, the density of the post-shock flow is decreased causing the reduction of pressure at PSC as well. In order to maintain the pressure balance across the standing shock in the presence of mass-loss, shock itself has to move inwards which is indicated by the solid vertical arrow. In panel (d), we plot the Mach number (M_j) variation of the outflowing matter with its radial coordinate (x_j) corresponding to panels (a), (b) and (c). The black filled circles represent the sonic locations and the arrows show the direction of motion of the outflowing matter. The inflow parameters for panel (a) are ($\mathcal{E}$, λ) = (0.007, 2.65), for (b) are (0.0025, 3.45) and for (c) are (0.0015, 4.0), respectively.

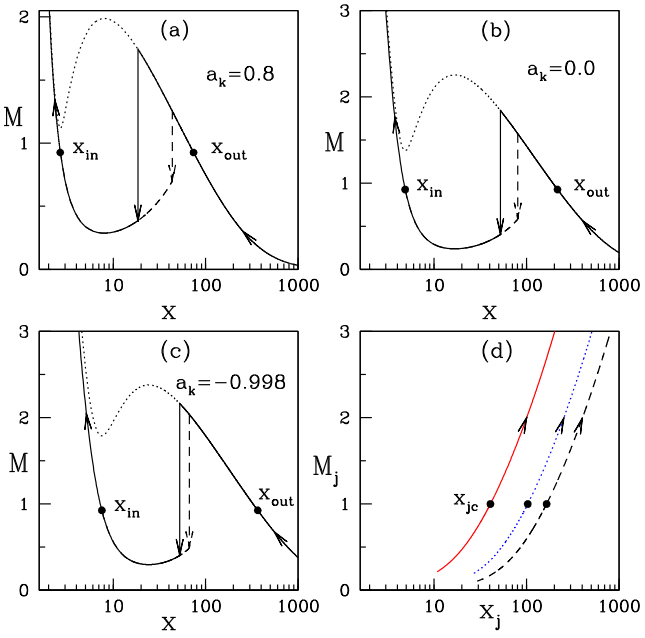

Figure 2. Variation of the inflowing Mach number M ($= v/a$) with radial distances (x) for (a) $a_k = 0.8$, (b) $a_k = 0$ and (c) $a_k = -0.998$, respectively. The corresponding outflow Mach number $M_j(=v_j/a_j)$ variation is shown in panel (d). See the text for details.

In Fig. 3, we compare the location of the shock transitions as a function of energy $\mathcal{E}$ for a set of angular momentum λ. In the upper panel, we choose $a_k = 0.6$ and find that the inflow–outflow solution possesses shock wave for a wide range of $\mathcal{E}$ and λ. As anticipated in Fig. 2, the shock location moves towards the BH horizon when $R_{\dot{m}} \neq 0$ just to maintain the pressure balance across

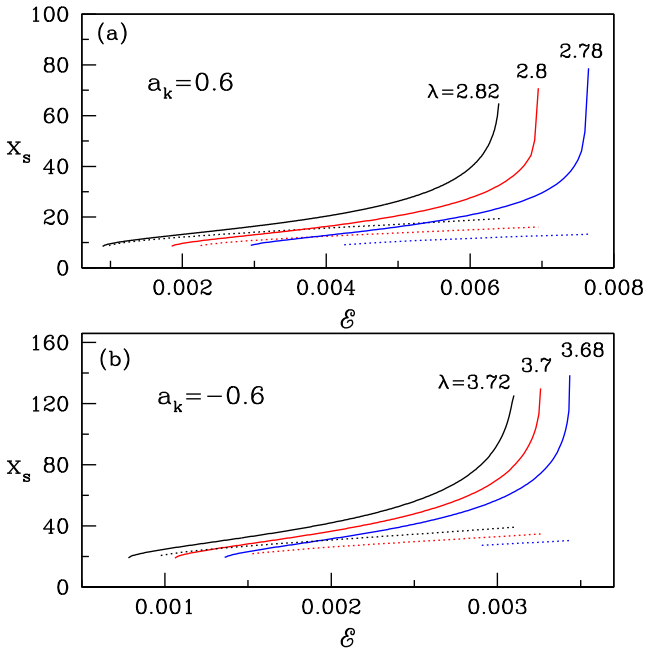

Figure 3. Variation of shock location as a function of energy $\mathcal{E}$. The solid curves represent results without mass-loss and the dotted curves are with mass-loss. In the upper panel, we choose $a_k = 0.6$, and curves are for $\lambda = 2.78$ (right), 2.80 (middle) and 2.82 (left), respectively. In the lower panel, we consider $a_k = -0.6$, and curves are for $\lambda = 3.68$ (right), 3.70 (middle) and 3.72 (left), respectively.

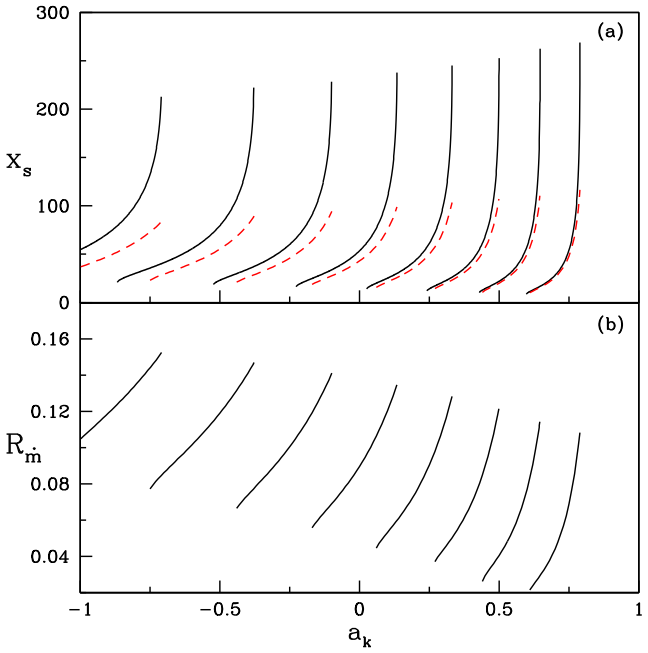

Figure 4. Variation of (a) shock location (x_s) and (b) outflow rate ($R_{\dot{m}}$) as a function of BH rotation parameter a_k for $\lambda = 2.8$–3.92 (right to left), where $\Delta\lambda = 0.16$. Here, we fixed the flow energy as $\mathcal{E} = 0.002$. In the upper panel, dashed curves denote the variation of shock location in the presence of outflow.

the shock. We again observe that the shock location reaches its lowest value around $x_s^{\min} \sim 8r_g$ at energies higher compared to the case of $R_{\dot{m}} = 0$ and the limiting value of this energy increases with the decrease of angular momentum of the flow. However, the maximum value of energy that allows shock transition in the presence of mass-loss is identical with no mass-loss case. This provides a clear hint that the range of inflow parameters for outflows, namely energy $\mathcal{E}$ and angular momentum λ, are reduced from their lower ends. In the lower panel, we consider $a_k = -0.6$ and obtained the similar results which differ only quantitatively. Overall, it is clear that the possibility of shock formation is affected substantially due to the presence of outflow.

Before we proceed further, we now investigate the effect of the BH rotation on the generation of mass outflow rate. In Fig. 4, we present the variation of shock location (x_s) and outflow rate ($R_{\dot{m}}$) as a function of a_k. Here, we fix $\mathcal{E} = 0.002$ and vary λ from 2.8 to 3.92 from the rightmost curve to the leftmost with an interval $\Delta\lambda = 0.16$. In the upper panel, the solid curves represent the shock locations in the absence of mass-loss. However, in the presence of mass-loss, accretion flow adjusts the location of the shock transition closer to the BH horizon in a way that the pressure balance condition across the shock is maintained which is depicted by the dashed curves. In contrast, as a_k is increased for a set of $\mathcal{E}$ and λ, the shock locations recede away from the BH horizon. This indicates that the size of the post-shock region (PSC) is enhanced with the increase of a_k and the inflowing matter is eventually intercepted by the large effective area of the post-shock flow that produces more outflow rate. In the lower panel, we present the feature of outflow rate variation with a_k. For a set of $\mathcal{E}$ and λ, the outflow rate $R_{\dot{m}}$ shows non-linear correlation for prograde as well as retrograde flows. In addition, we observe that for a given a_k, $R_{\dot{m}}$ is higher for increasing λ and with this, we infer that large outflow rate is associated with the higher λ and lower a_k

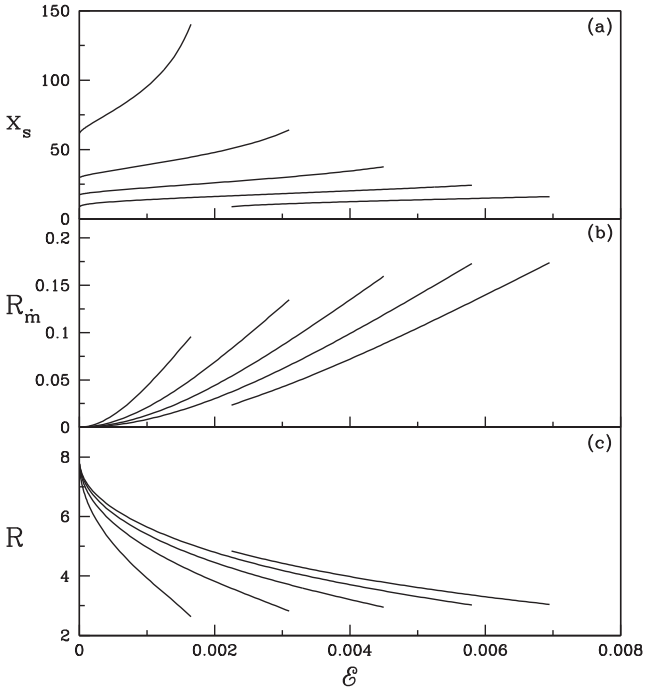

Figure 5. Variation of (a) shock location (x_s), (b) outflow rate ($R_{\dot{m}}$) and (c) compression ratio (R) as a function of energy $\mathcal{E}$ for $a_k = 0.6$, 0.65, 0.7, 0.75 and 0.8 (right to left). Here, we fix the flow angular momentum $\lambda = 2.8$.

when $\mathcal{E}$ is fixed. Overall, we find that the outflow rate reaches close to 16 per cent for these parameters as depicted in the figure.

Next, we study the characteristics of the post-shock quantities in terms of the inflow variables and present them in Fig. 5. Here, we choose the angular momentum as $\lambda = 2.8$ and vary energy $\mathcal{E}$ and BH

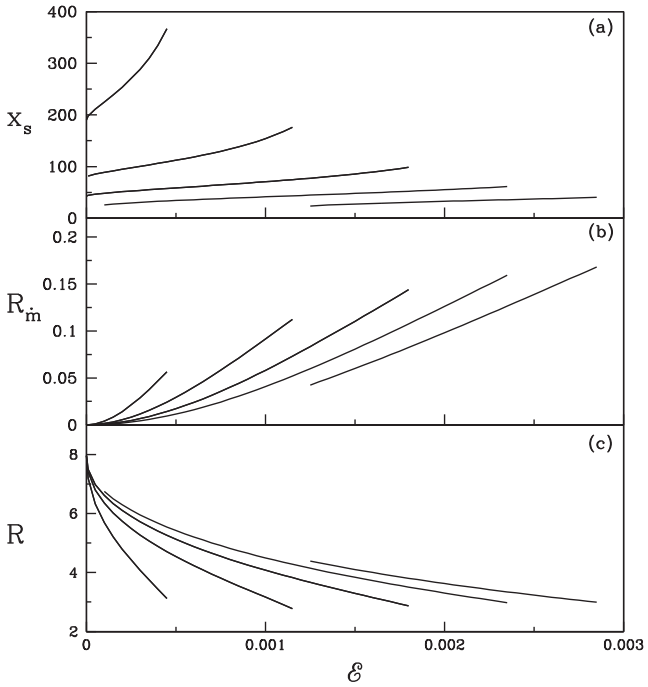

Figure 6. Same as Fig. 5. Here, $a_k = -0.998$, -0.8, -0.6, -0.4 and -0.2 (right to left), and flow angular momentum is $\lambda = 3.9$.

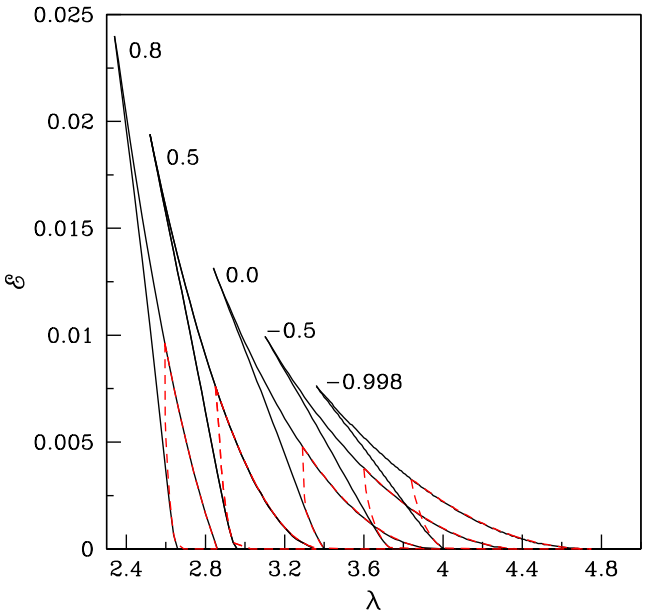

Figure 7. Energy angular momentum parameter space. Solid curve (black): shock parameter space without outflow. Dashed curve (red): shock parameter space with outflow. Various values of a_k are marked in the figure.

rotation parameter a_k. In the upper panel, we plot the variation of shock location (x_s) with $\mathcal{E}$ for a_k varied from 0.6 (right) to 0.8 (left) with $\Delta a_k = 0.05$. The corresponding variation of outflow rate $R_{\dot{m}}$ is shown in the middle panel. Due to shock transition, the post-shock flow is compressed. The measure of this compression is quantified as the ratio of the post-shock density to the pre-shock density, and it is termed as shock compression ratio R. In the lower panel, we present the variation of R with $\mathcal{E}$. When shock forms closer to the BH horizon, the amount of gravitational potential energy release is higher, ensuing the formation of strong shock. As the energy is increased, the shock location moves outwards that increases the outflow rate and weakens the shock compression ratio. We observe similar behaviour for all a_k. However, for a given λ and a_k, there is a range of energy beyond which mass outflow ceases to exist. This provides an indication of finding a parameter space for shock in the Fundamental Plane of energy and angular momentum of the inflow. We perform a similar study for retrograde flow as well and find the identical trend as depicted in Fig. 6.

As we pointed out earlier that the transonic accretion solutions including R-H shock waves are not isolated solutions. In fact, these solutions do exist for a wide range of parameters, namely energy ($\mathcal{E}$), angular momentum (λ) and BH rotation parameter (a_k). Towards this, we identify the shock-induced global accretion solutions using the parameter space spanned by the energy ($\mathcal{E}$) and angular momentum (λ) of the flow and classify them in terms of a_k. In Fig. 7, we separate the parameter spaces with the solid boundaries that indicate the regions for global shock accretion solutions in the absence of mass-loss. The corresponding values of a_k are marked in the figure. We further investigate the parameter spaces that cater mass-loss and indicate it with the dashed boundaries. Due to mass-loss, the post-shock region (PSC) shrinks as seen in Fig. 2, and therefore, the associated parameter space is reduced compared to the results having no outflows, particularly towards the lower energy and lower angular momentum sides (see Fig. 3). For flows with input parameters chosen from these parts of the parameter space, shock forms very close to the BH horizon when outflow is ignored (Das et al. 2001b) and they cease to exist when the outflow is allowed to emerge out from the post-shock disc.

So far, we have presented the shock-induced complete global inflow–outflow solutions and its properties for a given value of $\gamma = 4/3$. In reality, however, the theoretical limit of γ lies in the range between $4/3$ and $5/3$ depending on the ratio between the thermal energy and the rest energy of the flow (Frank, King & Raine 2002). To infer this, we consider rotating flows that are characterized as thermally ultra-relativistic ($\gamma \sim 4/3$), thermally trans-relativistic ($\gamma \sim 1.4$) and thermally semi-non-relativistic ($\gamma \sim 1.5$), respectively (Kumar et al. 2013), and obtain the parameter spaces for $a_k = 0.5$ similar to Fig. 7. This is shown in Fig. 8. Here, we observe that in all three cases shocks exist for a significant range of inflow parameters. However, the range of parameters for shock reduces considerably as the flow changes its ultra-relativistic character towards the non-relativistic limit. In addition, we find that all the parameter spaces further shrink as in Fig. 7, when a part of the inflowing matter is deflected in the form of mass-loss from the inner part of the disc (PSC).

According to the formalism adopted in this work, the mass outflow rate $R_{\dot{m}}$ is computed self-consistently in terms of the inflow parameters around a BH of rotation parameter a_k. This allows us to estimate the maximum $R_{\dot{m}}^{\max}$ for a given value of γ. While doing this, we identify a particular set of energy ($\mathcal{E}$) and angular momentum (λ) from their full range that provides the highest value of $R_{\dot{m}}$. The importance of this investigation is associated with the study of the maximum jet kinetic power corresponding to $R_{\dot{m}}^{\max}$, which we discuss in the next section. Following Fig. 8, we calculate the variation of $R_{\dot{m}}^{\max}$ as a function of a_k for various values of γ which is presented in Fig. 9. The results displayed in upper, middle and bottom panels are for $\gamma = 4/3$, 1.4 and 1.5, respectively. We find that $R_{\dot{m}}^{\max}$ gradually increases with the increase of a_k for all cases. We also observe that the accretion flows having $\gamma = 4/3$ have the potential to produce more outflows compared to the flows with higher values of γ. This is perhaps inevitable due to the fact that the outflows

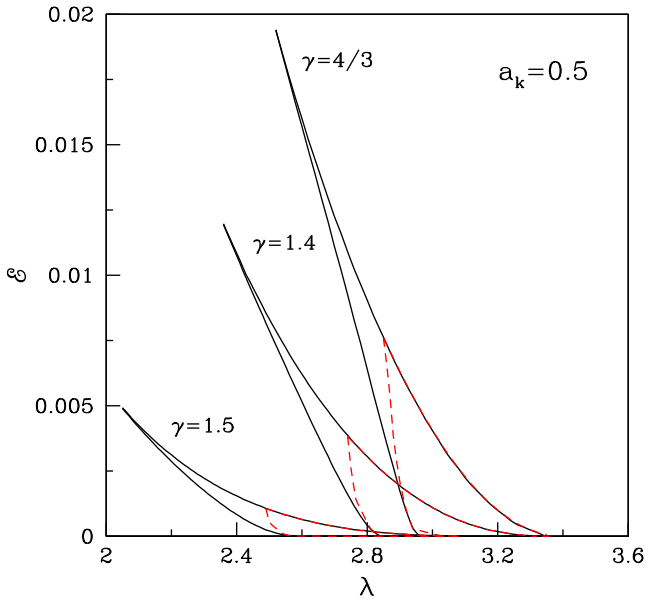

Figure 8. Effective regions of parameter space separated in terms of shock wave transition for various values of γ marked in the figure. Here, we choose $a_k = 0.5$. The solid boundary denotes the presence of shock waves in the absence of mass-loss and the dashed boundary represents the results including mass-loss.

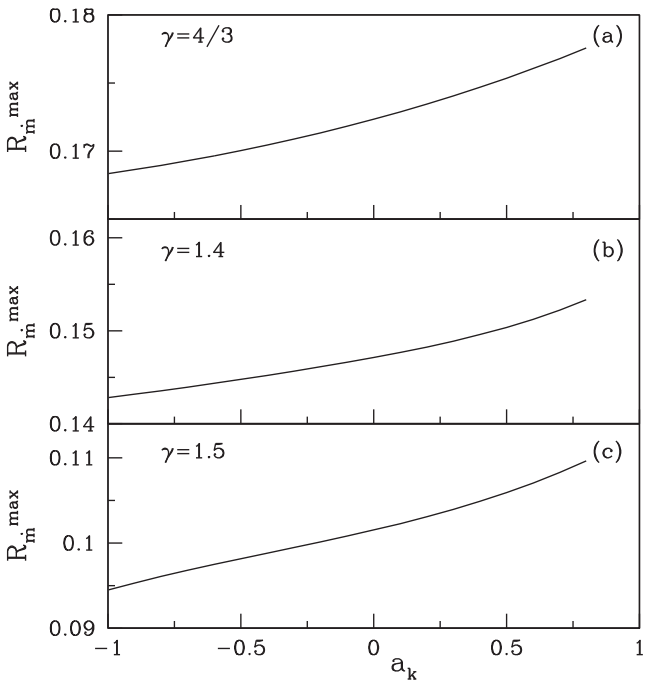

Figure 9. Variation of maximum outflow rates $R_{\dot{m}}^{\max}$ with the BH rotation parameter a_k. Upper panel is for $\gamma = 4/3$ (a), middle panel is for $\gamma = 1.4$ (b) and bottom panel is for $\gamma = 1.5$ (c), respectively. See the text for details.

under consideration are thermally driven and therefore, thermally ultra-relativistic flows exhibit maximum outflows. Following this, in the next section, we consider $\gamma = 4/3$ while computing the jet kinetic power for GBHs and AGNs, until otherwise stated.

Until now, we discuss the various properties of the accretion–ejection solutions in terms of the inflow parameters. However, all these studies are based on the assumption of stationary state

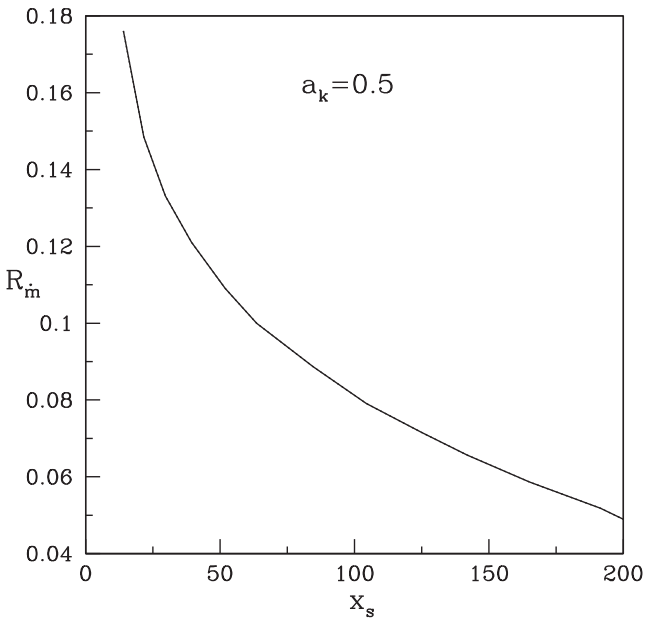

Figure 10. Variation of outflow rate ($R_{\dot{m}}$) with shock location (x_s) obtained for different sets of energy ($\mathcal{E}$) and angular momentum (λ). Here, $a_k = 0.5$ is used for representation. See the text for details.

that does not represent the dynamical behaviour of accretion flows around the outbursting BH sources. Usually, these sources change their accretion states with time, and the characteristic features of the emergent radiations and the jet properties are also varied accordingly. During these dynamical change of states, it is unlikely that the dissipative properties (i.e. viscosity, cooling processes, etc.) of the accretion flow will remain constant all throughout; instead, they seem to adjust in such a way that suitably represents the dynamical variation of PSC. In LHS of GBHs, the typical geometry of PSC is quite large which reduces considerably in HIMS as the dynamical shock moves towards the BH during the rising phase of the outburst. Such a trend has been reported while modelling the evolution of QPO frequencies for several BH sources (Chakrabarti et al. 2008; Chakrabarti, Dutta & Pal 2009; Nandi et al. 2012; Debnath, Chakrabarti & Nandi 2013; Radhika & Nandi 2014; Iyer, Nandi & Mandal 2015). Interestingly, it is also observed that most of the GBH sources show persistent/steady radio emission during these accretion states (Fender et al. 2004, 2009). Now, we attempt to address the evolution of accretion states from LHS to HIMS and its association with mass-loss using our present formalism as case by case which possibly acts as a local model at individual time frame. Towards this, a set of energy and angular momentum ($\mathcal{E}$, λ) of the inflowing matter is identified which would represent their local values for a dissipative accretion flow and obtain the shock location x_s and outflow rate $R_{\dot{m}}$ for a given a_k. Since the post-shock geometry (PSC) is associated with x_s, as anticipated earlier, we chose various such sets of ($\mathcal{E}$, λ) in a way that x_s moves towards the BH and show the variation of $R_{\dot{m}}$ with x_s in Fig. 10 for a typical value of $a_k = 0.5$. Note that $R_{\dot{m}}$ is increased with the decrease of x_s resulting in more jet kinetic power that represents the common characteristic of radio emissions observed in outbursting sources.

5 ASTROPHYSICAL APPLICATION

Here, we attempt to estimate the mass outflow rate and its associated jet kinetic power for various astrophysical BH sources (GBHs and

Table 1. Accretion state-dependent jet kinetic power.

Objects	$M_{\rm BH}$ ($M_\odot$)	d (kpc)	a_k	Observation (3–30 keV) States	$F_{\rm x}$ (erg cm^{-2} s^{-1})	$\dot{M}_{\rm acc}$ ($\dot{M}_{\rm Edd}$)[a]	$R_{\dot{m}}$ (per cent)	$L_{\rm jet}$ (erg s^{-1})	$L_{\rm jet}^{\rm Obs}$ [c] (erg s^{-1})
XTE J1859+226	7	11	0.4	LHS	5.71×10^{-9}	0.304	9.83	2.52×10^{37}	
(1999 Outburst)				HIMS	12.79×10^{-9}	0.680	17.5	1.08×10^{38}	
									1.82×10^{38} (1)
GRO J1655−40	6.3	3.2	0.7	LHS	3.19×10^{-9}	0.016	9.98	1.18×10^{36}	
(2005 Outburst)				HIMS	8.02×10^{-9}	0.040	17.68	5.79×10^{36}	
									3.01×10^{36} (2)
GX 339−4	7.5	15	0.4	LHS	15.71×10^{-9}	1.450	9.98	1.29×10^{38}	
(2002 Outburst)				HIMS[b]	12.12×10^{-9}	1.118	17.5	1.90×10^{38}	
									2.92×10^{38} (1)
H 1743−322	8	8.5	0.2	HIMS	4.03×10^{-9}	0.112	17.35	2.01×10^{37}	
(2009 Outburst)									1.08×10^{38} (3)
GRS 1915+105	12.4	8.6	>0.98[†]	LHS	20.33×10^{-9}	0.373	9.98	5.99×10^{37}	
(1997 Observation)									8.06×10^{37} (1)

Notes. [a] $\dot{M}_{\rm Edd} = 1.44 \times 10^{17} (\frac{M_{\rm BH}}{M_\odot})$g s^{-1}.

[b] Total flux in HIMS (3–30 keV) is smaller than LHS as the contribution of the hard X-ray flux (>10 keV) in HIMS is less.

[c] $L_{\rm jet}^{\rm Obs} = \eta \dot{M}_{\rm out} c^2$ is used for the source H 1743−322, where $\dot{M}_{\rm out}$ is the outflow rate (see reference). For other sources, $L_{\rm jet}^{\rm Obs} = L_r \times L_{\rm Edd}$ is used, where L_r is the observed jet power (in Edd) (see references) and $L_{\rm Edd} = 1.3 \times 10^{38} (\frac{M_{\rm BH}}{M_\odot})$erg s^{-1}.

References: (1) Fender et al. (2004), (2) Migliari et al. (2007), (3) Miller et al. (2012).

AGNs) using our present formalism. Since our work deals with the steady outflows, we focus only on those sources, particularly on their accretion states, where persistent/steady jets are observed. These jets are essentially compact (i.e. optically thick) in nature and are not isolated completely from the core of the central engine (Mirabel & Rodriguez 1994, 1998; Corbel et al. 2000, 2001; Fender et al. 2001).

5.1 Jet kinetic power predicted from accretion states

We consider five BH sources, namely XTE J1859+226, GRO J1655−40, GX 339−4, H 1743−322 and GRS 1915+105, respectively. For these sources, mass ($M_{\rm BH}$), distance (d) and spin (a_k) are constrained within the accuracy limit and are given in Table 1. In order to estimate the jet kinetic power, we calculate the X-ray flux for these sources in the LHS and HIMS using *RXTE*[1] satellite data.

In general, GBH sources undergo outbursts (Homan & Belloni 2005; Remillard & McClintock 2006; Debnath et al. 2008, 2013; Nandi et al. 2012; Radhika & Nandi 2014; Iyer et al. 2015) and show activity of radio emissions coupled with the accretion states of their evolution during the outburst phases (Brocksopp et al. 2002; Fender et al. 2004, 2009; Cadolle Bel et al. 2011; Miller-Jones et al. 2012; Radhika & Nandi 2014). It has also been observed that most of the outbursting sources show persistent/steady jet activity during LHS and HIMS, while transient 'relativistic' ejections are observed during the transition from HIMS to SIMS (Brocksopp et al. 2002; Fender et al. 2004, 2009; Radhika & Nandi 2014).

In order to estimate the 'model predicted' jet power based on accretion states, we estimated X-ray flux from a single observation of each state (i.e. LHS and HIMS) for all the sources from different outburst phases (as mentioned in Table 1). We use archival data obtained from the HEASARC data base of the *RXTE* satellite for the estimation of X-ray flux for all the five sources. We extracted and analysed background-subtracted PCA (3–30 keV) spectral data using PCU2 detector (i.e. well-calibrated detector) for our specific purpose. The standard FTOOLS package of HEASOFT v6.15.1 was used for spectral data reduction (see Nandi et al. 2012; Radhika & Nandi 2014 for details). For spectral analysis and modelling, we used the packages of XSPEC v12.8.1.

We have done spectral modelling for each observation from each spectral state (i.e. LHS and HIMS) for all the five sources using PCA spectral data in the energy range of 3–30 keV. We model the energy spectrum using the phenomenological accretion disc model, i.e. consisting of a *diskbb* and a *power-law* component. In this modelling, the *diskbb* and *power-law* components provide the contribution from the accretion disc and 'hot' Compton corona (i.e. PSC), and thereby one can estimate the total *unabsorbed* X-ray flux ($F_{\rm x}$, in units of erg cm^{-2} s^{-1}) emitted from the accretion disc around the GBH sources.

Once we obtain the *unabsorbed* X-ray flux ($F_{\rm x}$) of a source, we calculate the X-ray luminosity ($L_{\rm x}$) of the source employing the relation $L_{\rm x} = 4\pi d^2 F_{\rm x}$, where d is the distance of the source. Assuming that the maximum radiative efficiency of the infalling matter around rotating BH is $\eta \sim 0.3$, we calculate the accretion rate of the black hole as

$$\dot{M}_{\rm acc} = 2.99 \times 10^{-16} \left(\frac{F_{\rm x}\, d^2}{c^2}\right) \left(\frac{M_{\rm BH}}{M_\odot}\right)^{-1} \dot{M}_{\rm Edd}.$$

Here, $M_{\rm BH}$ denotes the mass of the black hole and $\dot{M}_{\rm Edd}$ represents the Eddington accretion rate. Next, we calculate the mass outflow rate using our theoretical estimate (equation 14) which has its maximum limit ($R_{\dot{m}}^{\rm max}$) for a particular set of (a_k, $\mathcal{E}$, λ) (see Fig. 9). With this, we find the *maximum mass outflow rate* as $\dot{M}_{\rm out} = R_{\dot{m}}^{\rm max} \dot{M}_{\rm acc}$ which successively allows us to compute the *maximum jet kinetic power* as

$$L_{\rm jet}^{\rm max} = R_{\dot{m}}^{\rm max} \times \dot{M}_{\rm acc} \times c^2 \ {\rm erg\ s^{-1}}. \quad (15)$$

As pointed out earlier, steady and persistent radio emissions are observed during LHS and HIMS (Fender et al. 2004, 2009). In addition, there are indications that the radio emission increases while the state transition from LHS to HIMS takes place. Moreover, the radio emission becomes non-steady during the HIMS itself just prior to the ejection and it is quite known that the relativistic

ejections take place during the transition from HIMS to SIMS (Fender et al. 2004, 2009). All these observations perhaps indicate that the persistent jet activity would be maximum during HIMS. Therefore, in order to study the outflow properties in the HIMS, we consider the maximum outflow rate obtained from our model calculation (see Fig. 9) and use it to estimate the jet kinetic power. On the other hand, jet kinetic power in the LHS is expected to be lower than that in the HIMS although its quantitative estimate is unclear. Therefore, we use outflow rate to be around ∼10 per cent as a representative value while calculating the jet kinetic power for LHS. Below, we mention the fundamental properties of each source and present the details for the estimation of jet kinetic power corresponding to individual states of a particular observation.

5.1.1 XTE J1859+226

Filippenko & Chornock (2001) first presented the dynamical estimate of mass of the source to be around $7.4 \pm 1.1\,\mathrm{M}_{\odot}$. Recently, Radhika & Nandi (2014) claimed that the mass of XTE J1859+226 is perhaps in between 6.58 and $8.84\,\mathrm{M}_{\odot}$ which is similar to the prediction of Shaposhnikov & Titarchuk (2009), although the lower mass limit is estimated as $5.4\,\mathrm{M}_{\odot}$ by Corral-Santana et al. (2011). However, we consider the typical mass of the source as $7\,\mathrm{M}_{\odot}$. The distance of this source is around $d \sim 11$ kpc (Filippenko & Chornock 2001). Steiner et al. (2013) measured the spin as $a_k \sim 0.4$; however, Motta et al. (2014b) recently reported that the spin of the source is $a_k \sim 0.34$. Since the spin predictions are quite close, we use $a_k \sim 0.4$ for this analysis. We estimate the fluxes $F_{\rm x}$ (see Table 1) of LHS and HIMS of the 1999 outburst of the source (Radhika & Nandi 2014). The corresponding disc luminosities are calculated as $L_{\rm disc}^{\rm LHS} = 8.26 \times 10^{37}$ erg s^{-1} and $L_{\rm disc}^{\rm HIMS} = 1.85 \times 10^{38}$ erg s^{-1}, respectively. Now, it is reasonable to assume the accretion efficiency for rotating BH as $\eta = 0.3$ which corresponds to the accretion rate of the inflowing matter as $\dot{M}_{\rm acc}^{\rm LHS} = 0.304\dot{M}_{\rm Edd}$ in LHS and $\dot{M}_{\rm acc}^{\rm HIMS} = 0.680\dot{M}_{\rm Edd}$ in HIMS. For LHS, we use $R_{\dot{m}} = 9.83$ per cent following our theoretical estimate where $x_{\rm s} = 64.6r_{\rm g}$ for $a_k = 0.4$, $\mathcal{E} = 0.001\,98$ and $\lambda = 3.18$. Incorporating these inputs in equation (15), we obtain the jet kinetic power as $L_{\rm jet}^{\rm LHS} = 2.52 \times 10^{37}$ erg s^{-1}. The maximum mass outflow rate for HIMS corresponding to $a_k = 0.4$ is obtained from Fig. 9 as $R_{\dot{m}}^{\rm max} = 17.5$ per cent for $\mathcal{E} = 0.005\,47$ and $\lambda = 3.1$, where the shock transition occurs at $21.9r_{\rm g}$. Using these values in equation (15), we obtain the maximum jet kinetic power as $L_{\rm jet}^{\rm HIMS} = 1.08 \times 10^{38}$ erg s^{-1} which we regard to be associated with the HIMS of this source.

5.1.2 GRO J1655−40

The mass of the source GRO J1655−40 is reported by Greene, Bailyn & Orosz (2001) and is given by $6.3\,\mathrm{M}_{\odot}$. Recently, Motta et al. (2014a) estimated the object mass as $5.31 \pm 0.07\,\mathrm{M}_{\odot}$. This source is located at around $d \sim 3.2$ kpc, and the spin of this source is estimated by Shafee et al. (2006) using *RXTE*[1] and *ASCA* data through the modelling of the thermal spectral continuum and obtained in the range $a_k \sim 0.65$–0.75 (and reference therein). Fitting the strong reflection features of iron line in *XMM–Newton* data, Reis et al. (2009) determine the lower limit of the spin of this object $a_k = 0.9$. Motta et al. (2014a) calculated the spin of the object using X-ray timing method and found it to be $a_k = 0.290 \pm 0.003$ which is an inconsistent estimate compared to iron line or continuum methods. In our present analysis, however, we consider $a_k = 0.7$. As before, we analysed the 2005 outburst of GRO J1655−40 to calculate the X-ray fluxes ($F_{\rm x}$) for LHS and HIMS (see Table 1) in the energy range 3–30 keV and obtain the corresponding accretion rates $\dot{M}_{\rm acc}^{\rm LHS} = 0.016\dot{M}_{\rm Edd}$ in LHS and $\dot{M}_{\rm acc}^{\rm HIMS} = 0.040\dot{M}_{\rm Edd}$ in HIMS. We use $R_{\dot{m}} = 9.98$ per cent in case of LHS which is obtained for $a_k = 0.7$, $\mathcal{E} = 0.002\,58$ and $\lambda = 2.845$, where $x_{\rm s} = 49.98r_{\rm g}$. From these values, we estimate jet kinetic power in LHS as $L_{\rm jet}^{\rm LHS} = 1.18 \times 10^{36}$ erg s^{-1}. For HIMS, we estimate the maximum mass outflow rate for $a_k = 0.7$ (see Fig. 9) as $R_{\dot{m}}^{\rm max} = 17.68$ per cent where $\mathcal{E} = 0.0073$ and $\lambda = 2.715$ with $x_{\rm s} = 16.73r_{\rm g}$. These inputs provide the maximum jet kinetic power as $L_{\rm jet}^{\rm HIMS} = 5.79 \times 10^{36}$ erg s^{-1}.

5.1.3 GX 339−4

The mass of the object is estimated as $7.5 \pm 0.8\,\mathrm{M}_{\odot}$ Chen (2011) and distance $d \sim 15$ kpc by Hynes et al. (2004). The issue of spin measurement of this objects is not settled yet as there are conflicting measurements. Analysing the *XMM–Newton* data set for broad iron line detection, Reis et al. (2008) and Miller et al. (2008) claimed $a_k = 0.935$ while the disc continuum fitting prefers the lower spin having upper limit of $a_k < 0.9$ (Kolehmainen & Done 2010). However, analysing the wide-band *Suzaku* spectra, Yamada et al. (2009) pointed out $a_k < 0.4$. Being aware of these, we consider a conservative estimate of spin as $a_k = 0.4$ in our calculation. This source has undergone outburst phases several times during *RXTE* era. For this analysis, we consider the 2002 outburst spectral data (in the energy band of 3–30 keV) for LHS and HIMS. During May 2 of the 2002 outburst, the object was in LHS emitting X-ray flux of $F_x^{\rm LHS} = 15.71 \times 10^{-9}$ erg cm^{-2} s^{-1} (see Table 1) and the disc luminosity of $L_{\rm disc}^{\rm LHS} = 4.22 \times 10^{38}$ erg s^{-1}. Using $\eta = 0.3$, the disc rate is calculated as $\dot{M}_{\rm acc}^{\rm LHS} = 1.450\dot{M}_{\rm Edd}$. Estimating $R_{\dot{m}} = 9.98$ per cent from our model using $\mathcal{E} = 0.001\,98$ and $\lambda = 3.18$ with $x_{\rm s} = 64.63r_{\rm g}$, we calculate the jet kinetic power as $L_{\rm jet}^{\rm LHS} = 1.29 \times 10^{38}$ erg s^{-1}. On May 12 of the 2002 outburst, the source was in HIMS and the radiated X-ray flux was calculated as $F_x^{\rm HIMS} = 12.12 \times 10^{-9}$ erg cm^{-2} s^{-1} (see Table 1) and the disc luminosity of $L_{\rm disc}^{\rm HIMS} = 3.26 \times 10^{38}$ erg s^{-1}. Using $\eta = 0.3$, the disc rate is calculated as $\dot{M}_{\rm acc}^{\rm HIMS} = 1.118\dot{M}_{\rm Edd}$. Estimating $R_{\dot{m}}^{\rm max} = 17.5$ per cent from our model using $\mathcal{E} = 0.00\,547$ and $\lambda = 3.1$ with $x_{\rm s} = 21.9r_{\rm g}$, we calculate the maximum jet kinetic power to be $L_{\rm jet}^{\rm HIMS} = 1.90 \times 10^{38}$ erg s^{-1}.

5.1.4 H 1743−322

Miller et al. (2012) and Steiner, McClintock & Reid (2012) reported the mass, distance and spin of H 1743−322 as $\sim 8\,\mathrm{M}_{\odot}$, $d \sim 8.5$ kpc and $a_k = 0.2$, respectively. Using the *RXTE* observation of the 2009 outburst of the source, the disc luminosity for this source is computed for the energy range of 3–30 keV corresponding to the measured X-ray flux of $F_x^{\rm HIMS} = 4.03 \times 10^{-9}$ erg cm^{-2} s^{-1} in HIMS (see Table 1) (Miller-Jones et al. 2012) as 4.63×10^{37} erg s^{-1}. Assuming $\eta = 0.3$, we obtain the accretion rate as $\dot{M}_{\rm acc}^{\rm HIMS} = 0.112\dot{M}_{\rm Edd}$. Accretion rate in LHS is not known due to lack of observation during the 2009 outburst (Miller-Jones et al. 2012). For $a_k = 0.2$, $\mathcal{E} = 0.004\,85$ and $\lambda = 3.176$, we obtain the maximum mass outflow rate for HIMS as $R_{\dot{m}}^{\rm max} = 17.35$ per cent with $x_{\rm s} = 23.66r_{\rm g}$. Employing these values, we find the maximum jet kinetic power as $L_{\rm jet}^{\rm HIMS} = 2.01 \times 10^{37}$ erg s^{-1}.

5.1.5 GRS 1915+105

Earlier, Greiner, Cuby & McCaughrean (2001) estimated the mass of GRS 1915+105 as (14 ± 4) $M_\odot$. Recently, Hurley et al. (2013) reported the new mass estimate as (12.9 ± 2.4) $M_\odot$ which is further revised as (12.4 ± 2) $M_\odot$ by Reid et al. (2014). The distance of the source is reported as $d \sim (9.4 \pm 0.2)$ kpc by Hurley et al. (2013), and Reid et al. (2014) claimed the distance to be $d \sim (8.6 \pm 2)$ kpc. However, in this calculation we use the mass and distance of the source as 12.4 $M_\odot$ and 8.6 kpc, respectively, in order to compute the disc luminosity. The source is extremely rotating as McClintock et al. (2006) estimated the spin parameter $a_k > 0.98$ which is similar to the estimate of Blum et al. (2009). As the source is highly variable in X-rays, we choose one observation when the source was in the *hard state* that is similar to LHS of other GBH sources. *RXTE* observed the source in the energy range of 3–30 keV on 1997 October 22 and the object was in so-called χ-class (Belloni, Méndez & Sánchez-Fernández 2001; Nandi, Manickam & Chakrabarti 2001c). For this observation, the disc luminosity corresponding to the X-ray flux of $F_x^{\rm LHS} = 20.33 \times 10^{-9}$ erg cm^{-2} s^{-1} (see Table 1) is obtained as 1.79×10^{38} erg s^{-1} which provides the disc accretion rate as $\dot{M}_{\rm in}^{\rm LHS} = 0.373 \dot{M}_{\rm Edd}$. According to our model, the mass outflow rate for LHS (or simply hard state for this source) is calculated as $R_{\dot{m}} = 9.98$ per cent, where $x_{\rm s} = 50.47 r_{\rm g}$ with $a_k = 0.98$, $\mathcal{E} = 0.002\,76$ and $\lambda = 2.679$. Here, we cross the upper limit of a_k (indicated by dagger (†) in column 4 of Table 1) as the adopted BH potential satisfactorily describes the space–time geometry for $a_k \lesssim 0.8$. However, we anticipate that the obtained $R_{\dot{m}}$ provides qualitative estimate that would not differ significantly from its exact value. Using these values, the jet kinetic power is found to be $L_{\rm jet}^{\rm LHS} = 5.99 \times 10^{37}$ erg s^{-1}.

In this section, we calculated the jet kinetic power mostly for outbursting GBH sources (except GRS 1915+105) for different accretion states (i.e. LHS and HIMS). Our findings clearly show that as the sources transit from LHS to HIMS, there is significant increase in the jet kinetic power. The predicted jet kinetic powers are in close agreement with the observed values for XTE J1859+226, GRO J1655−40, GX 339−4, GRS 1915+105 and H 1743−322 (Fender et al. 2004; Migliari et al. 2007; Miller et al. 2012).

5.2 Jet kinetic power estimated from accretion rates

We further extend our study to estimate the jet kinetic power for other GBH and AGN sources where we do not observe fast (∼ day-scale) state transitions similar to outbursting GBH sources (except XTE J1550−564). In order to calculate the jet kinetic power for these sources, we find their mass ($M_{\rm BH}$), accretion rate ($\dot{M}_{\rm acc}$) and spin (a_k) from the existing literature. Meanwhile, we compute $R_{\dot{m}}^{\rm max}$ corresponding to BH spin a_k using our theoretical approach. We then use the values of $\dot{M}_{\rm acc}$ and $R_{\dot{m}}^{\rm max}$ in equation (15) to estimate the jet kinetic power.

In Table 2, we display the physical parameters of the sources (GBHs and AGNs) under consideration along with the computed jet kinetic power obtained from our analysis. In columns 1–4, we present the list of sources, their mass ($M_{\rm BH}$), accretion rate ($\dot{M}_{\rm acc}$) and spin (a_k). In column 5 and 6, we mention the representative values of energy $\mathcal{E}$ and angular momentum λ of the inflow that provide the shock location $x_{\rm s}$ (in column 7) and the corresponding *maximum mass outflow rate* $R_{\dot{m}}^{\rm max}$ (in column 8). Finally, in column 9, we present the maximum jet kinetic power $L_{\rm jet}^{\rm max}$. The first seven sources are GBHs whereas the last three sources are AGNs. Here, we give emphasis on the maximum $R_{\dot{m}}$ in order to speculate the upper limit of jet kinetic power. We find that the estimated jet kinetic powers are in close agreement with the observed values at least for few sources, namely Cyg X-1, XTE J1550−564, M87 and Sgr A* (Falcke & Biermann 1999; Fender et al. 2004; de Gasperin et al. 2012). For remaining sources, we argue that the present method illustrates the typical estimates of jet kinetic power that possibly lie within the acceptable range. Further, in our analysis, we choose four sources having BH spin $a_k > 0.8$ which are indicated by dagger (†) in column 4. As before, we anticipate that the obtained $L_{\rm jet}^{\rm max}$ for these sources provide qualitative estimates that would not differ significantly from their observed values.

6 CONCLUDING REMARKS

In this work, we self-consistently examine the accretion–ejection mechanism around the rotating BHs. We consider the structure of the accretion disc to be stationary, thin, rotating and advection dominated which contains R-H shock waves. These shocks are formed as a consequence of CB located near the BH horizon. Based on the second law of thermodynamics, we argue that the shock solutions are dynamically preferred over the smooth solutions as they possess higher entropy (Becker & Kazanas 2001). During accretion, a part of the super-sonic matter is deflected at the CB due to excess thermal pressure caused by the shock compression and eventually emerges out in the form of thermally driven outflows. These outflows are further channelled through the confined geometry bounded by the FW and pressure maxima surface along the rotation axis of the BH (Molteni et al. 1996).

We find that mass-loss can occur for prograde as well as retrograde flows. When outflow is emerged out from the inner part of the disc (PSC), post-shock pressure is decreased that essentially compels the shock front to move forward towards the horizon in order to maintain the pressure balance across the shock. Therefore, a flow originally containing shock wave close to its minimum location ($x_{\rm s}^{\rm min}$) for $R_{\dot{m}} = 0$ will not provide any outflow as R-H shock conditions are not favourable there (see Fig. 3). This certainly tells us that the outflow solutions would be restricted compared to the global shocked accretion solutions in the absence of mass-loss. However, we show that the shock-induced global inflow–outflow solutions are not isolated solutions, but exist for a wide range of inflow parameters, namely $\mathcal{E}$ and λ, respectively. Interestingly, numerical simulations also indicate the similar findings as reported by Das et al. (2014). We examine the existence of such solutions with and without outflow and obtain the parameter space spanned by the $\mathcal{E}$ and λ as a function of BH rotation parameter a_k. As anticipated above, the parameter space that provides mass outflow is shrunk compared to the case of no outflow (see Fig. 7). In other words, a significant region of the parameter space that exhibits stationary shock for $R_{\dot{m}} = 0$ does not provide steady shock solutions in the presence of outflow. This possibly infers that the accreting matter having $\mathcal{E}$ and λ from this region of the parameter space may demonstrate the non-steady behaviour (Das et al. 2001b; Das 2007) which is triggered simply due to the presence of mass-loss. Investigation of such a scenario requires time-dependent calculations which is beyond the scope of the present work and we wish to report this elsewhere.

In this work, we mainly focused on thermally ultra-relativistic flows with adiabatic index $\gamma = 4/3$. However, when the cooling effects are negligible, the purely non-relativistic flow behaves like gas-pressure dominated with $\gamma \sim 5/3$. In reality, the value of γ would be an intermediate value depending on the dissipation processes active in the flow. Keeping this in mind, we calculate the

Table 2. Estimated jet kinetic power from accretion rate.

Objects	$M_{\rm BH}$ ($M_\odot$)	$\dot{M}_{\rm acc}$ ($\dot{M}_{\rm Edd}$)	a_k	$\mathcal{E}$ (c^2)	λ (cr_g)	x_s (r_g)	$R_{\dot{m}}^{\rm max}$ (per cent)	$L_{\rm jet}^{\rm max}$ (erg s^{-1})	$L_{\rm jet}^{\rm Obs}$ [a] (erg s^{-1})
A0620-00	6.60 (*a*)	1.684 (*b*)	0.12 (*b*)	0.004 44	3.25	26.84	17.25	2.48×10^{38}	–
LMC X-3	6.98 (*c*)	2.487 (*d*)	0.25 (*e*)	0.004 76	3.15	25.72	17.35	3.90×10^{38}	–
XTE J1550−564	9.10 (*f*)	0.511 (*g*)	0.34 (*g*)	0.005 30	3.06	22.07	17.43	1.05×10^{38}	3.55×10^{38} (*y*)
M33 X-7	15.66 (*h*)	0.718 (*i*)	0.84† (*j*)	0.008 07	2.61	15.60	17.79	2.59×10^{38}	–
4U 1543−47	9.40 (*k*)	1.315 (*l*)	0.43 (*l*)	0.005 65	2.98	21.07	17.48	2.80×10^{37}	–
LMC X-1	10.90 (*m*)	0.853 (*n*)	0.92† (*n*)	0.008 30	2.58	15.42	17.93	2.16×10^{37}	–
Cyg X-1	14.80 (*o*)	0.061 (*p*)	≥0.95† (*p*)	0.008 35	2.58	15.38	17.98	2.10×10^{37}	3.85×10^{37} (*y*)
Mrk 79	5.24×10^7 (*q*)	9.82×10^{-2} (*r*)	0.70 (*s*)	0.007 30	2.72	16.73	17.68	1.18×10^{44}	–
M87	3.50×10^9 (*t*)	1.16×10^{-4} (*u*)	≥0.65 (*v*)	0.007 05	2.76	16.94	17.62	9.25×10^{42}	1.00×10^{45} (*z*)
Sgr A*	4.90×10^6 (*w*)	7.89×10^{-5} (*x*)	0.99† (*w*)	0.008 59	2.57	14.71	18.09	9.07×10^{39}	1.00×10^{39} (*zz*)

Notes. [a] $L_{\rm jet}^{\rm Obs} = L_r \times L_{\rm Edd}$, where L_r is the observed jet power (in Edd) (see references).
References: (*a*) Cantrell et al. (2010), (*b*) Gou et al. (2010), (*c*) Orosz et al. (2014), (*d*) Kubota et al. (2010), (*e*) Steiner et al. (2014), (*f*) Orosz et al. (2011a), (*g*) Steiner et al. (2011), (*h*) Orosz et al. (2007), (*i*) Liu et al. (2008), (*j*) Liu et al. (2010), (*k*) Orosz (2003), (*l*) Morningstar & Miller (2014), (*m*) Orosz et al. (2009), (*n*) Gou et al. (2009), (*o*) Orosz et al. (2011b), (*p*) Gou et al. (2011), (*q*) Peterson et al. (2004), (*r*) Riffel, Storchi-Bergmann & Winge (2013), (*s*) Gallo et al. (2011), (*t*) Walsh et al. (2013), (*u*) Kuo et al. (2014), (*v*) Wang et al. (2008), (*w*) Aschenbach (2010), (*x*) Yuan, Markoff & Falcke (2002), (*y*) Fender et al. (2004), (*z*) de Gasperin et al. (2012), (*zz*) Falcke & Biermann (1999).

parameter space for different values of γ and find that shock forms in all the cases even in the presence of outflow. Interestingly, we observe that the effective region of the parameter space is reduced with the increase of γ indicating the limited possibility of shock transition when the flow changes its character towards the non-relativistic regime.

We have estimated the mass outflow rate using the inflow parameters, such as $\mathcal{E}$ and λ. We show that $R_{\dot{m}}$ increases with a_k for a fixed $\mathcal{E}$ and λ (see Fig. 4). This is possibly due to the fact that as a_k is increased, shock forms away from the BH. Therefore, the effective area of the post-shock flow (PSC), where the inflowing matter deflects to generate outflow, becomes large and results in enhanced outflow rate. Further, we attempt to find the maximum mass-loss ($R_{\dot{m}}^{\rm max}$) from the disc and quantify it in terms of the inflow parameters. For this, we fix the value of γ and explore all possible combinations of energy and angular momentum to obtain $R_{\dot{m}}^{\rm max}$. In Fig. 9, we show the variation of $R_{\dot{m}}^{\rm max}$ with a_k and observe that flow with $\gamma = 4/3$ exhibits the highest outflow rate $R_{\dot{m}}^{\rm max}$ that lies in the range around ∼17–18 per cent. Also, very weak correlation is seen between $R_{\dot{m}}^{\rm max}$ and a_k in all the cases. Moreover, we have shown in Fig. 10 that for various sets of ($\mathcal{E}$, λ), $R_{\dot{m}}$ increases with the decrease of x_s (equivalently jet power increases as the size of the PSC is reduced) based on the realistic scenario (i.e. spectral states transit from LHS to HIMS) which seems to be a common characteristic observed in GBH sources.

We employ our formalism in order to estimate the jet kinetic power ($L_{\rm jet}$) of several BH sources (GBHs and AGNs). To begin with, we consider outbursting sources to calculate $L_{\rm jet}$ based on the accretion states. For these sources, we compute their *unabsorbed* X-ray fluxes in LHS and HIMS using the data of *RXTE* observation and obtain their disc rate considering the accretion efficiency $\eta = 0.3$ which seems to be relevant for rotating BHs. Then, we calculate the outflow rate using our formalism and employ it in equation (15) along with the disc rate to obtain $L_{\rm jet}$. While estimating the jet kinetic power, we consider maximum outflow rate $R_{\dot{m}}^{\rm max}$ for HIMS (see Fig. 9) and $R_{\dot{m}} \sim 10$ per cent for LHS, as discussed in Section 5. In Table 1, we summarize the physical parameters of five BH sources along with the computed jet kinetic power. In the process of estimating $L_{\rm jet}^{\rm max}$, two quantities play major role. First one is the unabsorbed X-ray flux computed from *RXTE* archival data and the other is the maximum outflow rate obtained from our model calculation. We find that the estimated $L_{\rm jet}^{\rm max}$ for various sources are in close agreement with the observed values (Fender et al. 2004; Miller et al. 2012). We further extend our study for other BH sources where the fast accretion state transitions (∼ day scale) are not seen (except XTE J1550−564). For these sources, the disc rate is obtained from the existing literature (see Table 2) and $R_{\dot{m}}^{\rm max}$ is computed from our theoretical calculation which finally provides the $L_{\rm jet}^{\rm max}$. We present these results in Table 2. We notice that estimated $L_{\rm jet}^{\rm max}$ for Cyg X-1, XTE J1550−564, M87 and Sgr A* are also in close agreement with the observed values (Falcke & Biermann 1999; Fender et al. 2004; de Gasperin et al. 2012). Following this finding, we argue that $L_{\rm jet}^{\rm max}$ for rest of the sources would also in turn render the representative values which are expected to be consistent with their actual estimates.

The present work has limitations as it is developed based on some approximations. We use pseudo-Kerr gravitational potential to mimic the general relativistic effect around rotating BH that allows us to examine the properties of non-linear shock solutions in the presence of mass-loss in a simpler way. We ignore the effect of viscosity and radiative processes. We consider constant adiabatic index instead of calculating it self-consistently based on its thermal properties. Needless to mention that we have not addressed the issue of transient relativistic ejections and its collimation mechanism as we consider the jet geometry only up to its sonic point. Although the implementation of all such issues is beyond the scope of this paper, however, we believe that the above approximations will not alter our basic conclusions qualitatively.

ACKNOWLEDGEMENTS

We thank the reviewer for suggestions and comments that help us to improve the manuscript. We would like to thank Indranil Chattopadhyay and Samir Mandal for discussions. This research has made use of the data obtained through High Energy Astrophysics Science Archive Research Center on-line service, provided by NASA/Goddard Space Flight Center. AN acknowledges Group Director, SAG, Deputy Director, CDA and Director, ISAC, for continuous support to carry out this research at ISAC, Bangalore.

REFERENCES

Aschenbach B., 2010, Mem. Soc. Astron. Ital., 81, 319
Becker P. A., Kazanas D., 2001, ApJ, 546, 429
Belloni T., Méndez M., Sánchez-Fernández C., 2001, A&A, 372, 551
Blandford R. D., Znajek R. I., 1977, MNRAS, 179, 433
Blum J. L., Miller J. M., Fabian A. C., Miller M. C., Homan J., van der Klis M., Cackett E. M., Reis R. C., 2009, ApJ, 706, 60
Brocksopp C. et al., 2002, MNRAS, 331, 765
Cadolle B. M. et al., 2011, A&A, 534, 119
Cantrell A. G. et al., 2010, ApJ, 710, 1127
Chakrabarti S. K., 1989, ApJ, 347, 365
Chakrabarti S. K., 1990, Theory of Transonic Astrophysical Flows. World Scientific Press, Singapore
Chakrabarti S. K., 1999, A&A, 351, 185
Chakrabarti S. K., Manickam S., 2000, ApJ, 531, 41
Chakrabarti S. K., Mondal S., 2006, MNRAS, 369, 976
Chakrabarti S. K., Nandi A., Manickam S. G., Mandal S., Rao A. R., 2002, ApJ, 579, L21
Chakrabarti S. K., Debnath D., Nandi A., Pal P. S., 2008, A&A, 489, L41
Chakrabarti S. K., Dutta B. G., Pal P. S., 2009, MNRAS, 394, 1463
Chattopadhyay I., Das S., 2007, New Astron., 12, 454
Chen T., 2011, in Romero G., Sunyaev R., Bellon T., eds, Proc. IAU Symp. 275, Jets at All Scales. Cambridge Univ. Press, Cambridge, p. 327
Cheung C. C., 2002, ApJ, 581, 15
Corbel S., Fender R. P., Tzioumis A. K., Nowak M., McIntyre V., Durouchoux P., Sood R., 2000, A&A, 359, 251
Corbel S. et al., 2001, ApJ, 554, 43
Corral-Santana J. M., Casares J., Shahbaz T., Zurita C., Martínez-Pais I. G., Rodríguez-Gil P., 2011, MNRAS, 413, L15
Das S., 2007, MNRAS, 376, 1659
Das S., Chattopadhyay I., 2008, New Astron., 549, 556
Das S., Chattopadhyay I., Nandi A., Chakrabarti S. K., 2001a, A&A, 379, 683
Das S., Chattopadhyay I., Chakrabarti S. K., 2001b, ApJ, 557, 983
Das S., Chattopadhyay I., Nandi A., Molteni D., 2014, MNRAS, 442, 251
de Gasperin F. et al., 2012, A&A, 547, 56
De Villiers J. P., Hawley J. F., Krolik J. H., Hirose S., 2005, ApJ, 620, 878
Debnath D., Chakrabarti S. K., Nandi A., Mandal S., 2008, BASI, 36, 151
Debnath D., Chakrabarti S. K., Nandi A., 2013, Adv. Space Res., 52, 2143
Donea A. C., Biermann P. L., 1996, A&A, 316, 43
Falcke H., Biermann P. L., 1999, A&A, 342, 49
Fender R. P., Gallo E., 2014, Space Sci. Rev., 183, 323
Fender R. P., Hjellming R. M., Tilanus R. P. J., Pooley G. G., Deane J. R., Ogley R. N., Spencer R. E., 2001, MNRAS, 322, L23
Fender R. P., Belloni T., Gallo E., 2004, MNRAS, 355, 1105
Fender R. P., Homan J., Belloni T., 2009, MNRAS, 396, 1307
Fernández R., Kasen D., Metzger B. D., Quataert E., 2015, MNRAS, 446, 750
Feroci M., Matt G., Pooley G., Costa E., Tavani M., Belloni T., 1999, A&A, 351, 985
Ferrari A., 1998, ARA&A, 36, 539
Filippenko A. V., Chornock R., 2001, IAU Circ., 7644, 2
Frank I., King A. R., Raine D., 2002, Accretion Power in Astrophysics. Cambridge Univ. Press, Cambridge
Fukue J., 1987, PASJ, 39, 309
Fukumura K., Tsuruta S., 2004, ApJ, 611, 964
Gallo E., Fender R. P., Pooley G. G., 2003, MNRAS, 344, 60
Gallo L. C., Miniutti G., Miller J. M., Brenneman L. W., Fabian A. C., Guainazzi M., Reynolds C. S., 2011, MNRAS, 411, 607
Gou L. et al., 2009, ApJ, 701, 1076
Gou L., McClintock J. E., Steiner J. F., Narayan R., Cantrell A. G., Bailyn C. D., Orosz J. A., 2010, ApJ, 718, L122
Gou L. et al., 2011, ApJ, 742, 85
Greene J., Bailyn C. D., Orosz J. A., 2001, ApJ, 554, 1290
Greiner J., Cuby J. G., McCaughrean M. J., 2001, Nature, 414, 522
Hjellming R. M., Rupen M. P., 1995, Nature, 375, 464
Homan J., Belloni T., 2005, Ap&SS, 300, 107
Hurley D. J., Callanan P. J., Elebert P., Reynolds M. T., 2013, MNRAS, 430, 1832
Hynes R. I., Steeghs D., Casares J., Charles P. A., O'Brien K., 2004, ApJ, 609, 317
Iyer N., Nandi A., Mandal S., 2015, ApJ, 807, 108
Junor W., Biretta J. A., Livio M., 1999, Nature, 401, 891
Koide S., Shibata K., Kudoh T., Meier D. L., 2002, Science, 295, 1688
Kolehmainen M., Done C., 2010, MNRAS, 406, 2206
Kubota A., Done C., Davis S. W., Dotani T., Mizuno T., Ueda Y., 2010, ApJ, 714, 860
Kumar R., Chattopadhyay I., 2013, MNRAS, 430, 386
Kumar R., Singh C. B., Chattopadhyay I., Chakrabarti S. K., 2013, MNRAS, 436, 2864
Kuo C. Y. et al., 2014, ApJ, 783, L33
Landau L. D., Lifshitz E. D., 1959, Fluid Mechanics. Pergamon, New York
Liu J., McClintock J. E., Narayan R., Davis S. W., Orosz J. A., 2008, ApJ, 679, L37
Liu J., McClintock J. E., Narayan R., Davis S. W., Orosz J. A., 2010, ApJ, 719, L109
Lu J. F., Gu W. M., Yuan F., 1999, ApJ, 523, 340
McClintock J. E., Shafee R., Narayan R., Remillard R. A., Davis S. W., Li L.-X., 2006, ApJ, 652, 518
McClintock J. E., Narayan R., Steiner J., 2014, Space Sci. Rev., 183, 295
Machida M., Hayashi M. R., Matsumoto R., 2000, ApJ, 532, 67
McKinney J. C., Gammie C. F., 2004, ApJ, 611, 977
Migliari A. et al., 2007, ApJ, 670, 610
Miller J. M. et al., 2008, ApJ, 679, 113
Miller J. M. et al., 2012, ApJ, 759, L6
Miller-Jones J. C. A. et al., 2012, MNRAS, 421, 468
Mirabel I. F., 2003, New Astron. Rev., 47, 471
Mirabel I. F., Rodriguez L. F., 1994, Nature, 371, 46
Mirabel I. F., Rodriguez L. F., 1998, Nature, 392, 673
Mirabel I. F., Rodriguez L. F., Cordier B., Paul J., Lebrun F., 1992, Nature, 358, 215
Molteni D., Lanzafame G., Chakrabarti S. K., 1994, ApJ, 425, 161
Molteni D., Ryu D., Chakrabarti S. K., 1996, ApJ, 470, 460
Morningstar W. R., Miller J. M., 2014, ApJ, 793, 33
Motta S. E., Belloni T. M., Stella L., Muñoz-Darias T., Fender R., 2014a, MNRAS, 437, 2554
Motta S. E., Muñoz-Darias T., Sanna A., Fender R., Belloni T., Stella L., 2014b, MNRAS, 439, L65
Nandi A., Manickam S. G., Rao A. R., Chakrabarti S. K., 2001a, MNRAS, 324, 267
Nandi A., Chakrabarti S. K., Vadawale S. V., Rao A. R., 2001b, A&A, 380, 245
Nandi A., Manickam S. G., Chakrabarti S. K., 2001c, preprint (astro-ph/0012523)
Nandi A., Debnath D., Mandal S., Chakrabarti S. K., 2012, A&A, 542, A56
Okuda T., 2014, MNRAS, 441, 2354
Okuda T., Das S., 2015, MNRAS, 453, 147
Orosz J. A., 2003, in van der Hucht K. A., Esteban C., eds, Proc. IAU Symp.212, A Massive Star Odyssey: From Main Sequence to Supernova. Cambridge Univ. Press, Cambridge, p. 365
Orosz J. A. et al., 2007, Nature, 449, 872
Orosz J. A. et al., 2009, ApJ, 697, 573
Orosz J. A., Steiner J. F., McClintock J. E., Torres M. A. P., Remillard R. A., Bailyn C. D., Miller J. M., 2011a, ApJ, 730, 75
Orosz J. A., McClintock J. E., Aufdenberg J. P., Remillard R. A., Reid M. J., Narayan R., Gou L., 2011b, ApJ, 742, 84
Orosz J. A., Steiner J. F., McClintock J. E., Buxton M. M., Bailyn C. D., Steeghs D., Guberman A., Torres M. A. P., 2014, ApJ, 794, 154
Paczyński B., Wiita P., 1980, A&A, 88, 23
Penrose R., 1969, Riv. Nuovo Cimento, 1, 252
Peterson B. M. et al., 2004, ApJ, 613, 682
Radhika D., Nandi A., 2014, Adv. Space Res., 54, 1678
Reid M. J., McClintock J. E., Steiner J. F., Steeghs D., Remillard R. A., Dhawan V., Narayan R., 2014, ApJ, 796, 2

Reis R. C., Fabian A. C., Ross R. R., Miniutti G., Miller J. M., Reynolds C., 2008, MNRAS, 387, 1489
Reis R. C., Fabian A. C., Ross R. R., Miller J. M., 2009, MNRAS, 395, 1257
Remillard R. A., McClintock J. E., 2006, ARA&A, 44, 49
Riffel R. A., Storchi-Bergmann T., Winge C., 2013, MNRAS, 430, 2249
Rushton A., Spencer R., Fender R., Pooley G., 2010, A&A, 524, A29
Russell D. M., Gallo E., Fender R. P., 2013, MNRAS, 431, 405
Shafee R., McClintock J. E., Narayan R., Davis S. W., Li L.-X., Remillard R. A., 2006, ApJ, 636, L113
Shaposhnikov N., Titarchuk L., 2009, ApJ, 699, 453
Singh C. B., Chakrabarti S. K., 2011, MNRAS, 410, 2414
Steiner J. F. et al., 2011, MNRAS, 416, 941
Steiner J. F., McClintock J. E., Reid M. J., 2012, ApJ, 745, L7
Steiner J. F., McClintock J. E., Narayan R., 2013, ApJ, 762, 104
Steiner J. F., McClintock J. E., Orosz J. A., Remillard R. A., Bailyn C. D., Kolehmainen M., Straub O., 2014, ApJ, 793, L29
Thorne K. S., 1974, ApJ, 191, 507
Vadawale S. V., Rao A. R., Nandi A., Chakrabarti S. K., 2001, A&A, 370, L17
van Velzen S., Falcke H., 2013, A&A, 557, L7
Walsh J. L., Barth A. J., Ho L. C., Sarzi M., 2013, ApJ, 770, 86
Wang J. M., Li Y.-R., Wang J.-C., Zhang S., 2008, ApJ, 676, L109
Yamada S. et al., 2009, ApJ, 707, L109
Yuan F., Markoff S., Falcke H., 2002, A&A, 383, 854

This paper has been typeset from a TEX/LATEX file prepared by the author.